Helicity-Controlled Spin Hall Angle in 2D Altermagnets with Rashba Spin-Orbit Coupling

Weiwei Chen[1], Longhai Zeng[2], and W. Zhu[3*]

[1]*Key Laboratory of Intelligent Manufacturing Quality Big Data Tracing and Analysis of Zhejiang Province, College of Sciences, China Jiliang University, Hangzhou 310018, China*
[2]*Key Laboratory of Intelligent Manufacturing Quality Big Data Tracing and Analysis of Zhejiang Province, College of Science, China Jiliang University, Hangzhou 310018, China*
[3]*School of Science, Westlake University, Hangzhou 310024, China*

(Received 5 September 2024; accepted manuscript online 29 November 2024)

We investigated the efficiency of charge-to-spin conversion in two-dimensional Rashba altermagnets, a class of materials that combines the characteristics of both ferromagnets and antiferromagnets. Using quantum linear response theory, we quantified the longitudinal and spin Hall conductivities in this system and demonstrated a substantial enhancement in the spin Hall angle below the band crossing point through the dual effects of relativistic spin–orbit interaction and nonrelativistic altermagnetic exchange interaction. Additionally, the results showed that the skew scattering and intrinsic mechanisms arising from Fermi sea states are almost negligible in this system, in contrast to conventional ferromagnetic Rashba systems. Our findings not only elucidate the spin dynamics in Rashba altermagnets but also pave the way for developing novel strategies for manipulating charge-to-spin conversion via sophisticated control of noncollinear and collinear out-of-plane spin textures.

DOI: 10.1088/0256-307X/42/1/017201 CSTR: 32039.14.0256-307X.42.1.017201

Introduction. Altermagnets are an emerging class of magnetic materials exhibiting hybrid properties, bridging the gap between traditional ferromagnets and antiferromagnets.[1–10] These materials have attracted significant attention because of their promising applications in spintronics, particularly in the conversion between charge and spin.[11–16] Notable experimental observations include the out-of-plane spin torque induced by the in-plane charge current without an external magnetic field,[15] spin-to-charge conversion stemming from the altermagnetic spin-splitting effect,[7] and spin-current generation arising from anisotropic spin-split bands.[11,12] Therefore, the exploration of methods for improving the efficiency of these conversion processes is an important research endeavor.

Previous research on altermagnets has primarily focused on anisotropic antiparallel spin states;[16–20] however, the spin–orbit coupling (SOC) effect observed in most magnetic materials can substantially alter the spin directions of quasiparticles.[18,21,22] The interplay between nonrelativistic collinear spin splitting, driven by altermagnetic exchange interactions, and relativistic noncollinear spin splitting, induced by SOC, significantly enriches the spin textures in the crystal momentum space.[9] The spin texture plays a crucial role in quantum transport because it fundamentally shapes the electronic properties of materials and provides a fertile ground for engineering spin-dependent scattering processes, which are essential for advanced applications in spintronics.[23–28] By manipulating these spin textures, specific transport channels can be selectively enhanced or suppressed, thereby enabling precise control over the spin Hall effect and enhancing the efficiency of spin-current generation.[29,30]

In this study, we focused on charge and spin transport in a two-dimensional (2D) altermagnet with a Rashba-type SOC. Although Rashba SOCs produce helical in-plane spin textures,[31] alternating magnetic exchange interactions drive anisotropic out-of-plane spin polarization. In a typical 2D electron gas with a Rashba SOC, the spin Hall conductivity is zero for arbitrary values of electron density when only spin-conserving scattering is observed.[32–34] However, by calculating the longitudinal and spin Hall conductivities within the framework of quantum linear theory, we found that 2D altermagnets with Rashba SOCs exhibit finite spin Hall conductivity, and the ladder-type vertex correction, which corresponds to side-jump scattering, has the opposite effect on the spin Hall angle below and above the Dirac point.

Our findings revealed that the side-jump mechanism significantly influences the spin Hall angle, depending on the Fermi level relative to the band-crossing point, also called the Dirac point. When the Fermi level is above the Dirac point, the polarization direction of the out-of-plane spin in the backward-scattering states is parallel to that in the forward-scattering states; however, these directions are antiparallel when the Fermi level is below the Dirac point. Consequently, suppressing backward scattering via the side-jump mechanism below the Dirac point not only

*Corresponding author. Email: zhuwei@westlake.edu.cn
© 2025 Chinese Physical Society and IOP Publishing Ltd. All rights, including for text and data mining, AI training, and similar technologies, are reserved.

increases the distribution of transport states but also enhances spin polarization. This dual-enhancement effect significantly boosts the spin Hall conductivity, markedly increasing the spin Hall angle. Our results not only advance the understanding of spin dynamics in altermagnets with SOCs but also provide practical strategies for improving spintronic device functionalities through tailored spin texture manipulations.

Model. The low-energy effective Hamiltonian for a 2D altermagnet subject to a Rashba SOC is described as follows:[3–5]

$$H = tk^2 + 2t_J k_x k_y \sigma_z + \lambda(k_x\sigma_y - k_y\sigma_x). \tag{1}$$

Here, $\boldsymbol{k} = (k_x, k_y)$ represents the planar momentum, and σ_i $(i = x, y, z)$ are Pauli matrices. The first term represents conventional kinetic energy hopping, with parameter t serving as the energy unit in the subsequent calculations. The second term reflects the anisotropic exchange interaction in the altermagnetic state, which is characterized by the strength parameter t_J. The final term describes a Rashba SOC with strength λ. The quasiparticle state can be expressed as follows:

$$|\boldsymbol{k}+\rangle = \begin{pmatrix} \cos\frac{\theta}{2} \\ \sin\frac{\theta}{2}\mathrm{e}^{\mathrm{i}\phi} \end{pmatrix} \quad \text{and} \quad |\boldsymbol{k}-\rangle = \begin{pmatrix} \sin\frac{\theta}{2} \\ -\cos\frac{\theta}{2}\mathrm{e}^{\mathrm{i}\phi} \end{pmatrix}. \tag{2}$$

Here, the dispersion relation is denoted by $E_{\boldsymbol{k}\gamma} = tk^2 + \gamma d$, where (d, θ, ϕ) are the spherical coordinates of the vector $\boldsymbol{d} = (-\lambda k_y, \lambda k_x, 2t_J k_x k_y)$, and the index $\gamma = \pm 1$ distinguishes quasiparticle states at two different subbands.

Figure 1 shows the dispersion relations and spin textures of the effective model in Eq. (1). The spin texture of each quasiparticle state $|\boldsymbol{k}\lambda\rangle$ is quantified as $\langle s_i\rangle = \langle \boldsymbol{k}\gamma|\sigma_i|\boldsymbol{k}\gamma\rangle\hbar/2$. The two subbands ($\gamma = \pm 1$) intersect at $E = 0$, defining the Dirac point around which the Fermi surface splits into two distinct Fermi circles. In this case, both the in-plane and out-of-plane spin degeneracies are lifted. Specifically, the in-plane spin component $\langle s_\parallel\rangle$ exhibits helicity induced by SOC, and the out-of-plane component $\langle s_z\rangle$ exhibits pronounced anisotropic spin polarization, which is a manifestation of altermagnetism.

The charge velocities along the x- and y-directions of the Hamiltonian Eq. (1) are given by

$$\begin{aligned} v_x &= 2tk_x + 2t_J k_y\sigma_z + \lambda\sigma_y, \\ v_y &= 2tk_y + 2t_J k_x\sigma_z - \lambda\sigma_x. \end{aligned} \tag{3}$$

The corresponding spin velocities, which refer to the effective velocities at which the spin state contributes to the transport properties of a material, are defined as

$$\begin{aligned} v_{s,x} &= \frac{1}{2}\{v_x, \sigma_z\} = 2tk_x\sigma_z + 2t_J k_y\sigma_0, \\ v_{s,y} &= \frac{1}{2}\{v_y, \sigma_z\} = 2tk_y\sigma_z + 2t_J k_x\sigma_0. \end{aligned} \tag{4}$$

The disorder potential is modeled using randomly located δ-function scatterers, $V(\boldsymbol{r}) = \sum_i V_i\delta(\boldsymbol{r} - \boldsymbol{R}_i)$, where the average scattering strengths are characterized by $\langle V_i\rangle = 0$, $\langle V_i^2\rangle = V_0^2$, and $\langle V_i^3\rangle = V_1^3$. The second and third moments, $\langle V_i^2\rangle$ and $\langle V_i^3\rangle$, are crucial for quantifying the contributions of the side-jump and skew scattering mechanisms.[35]

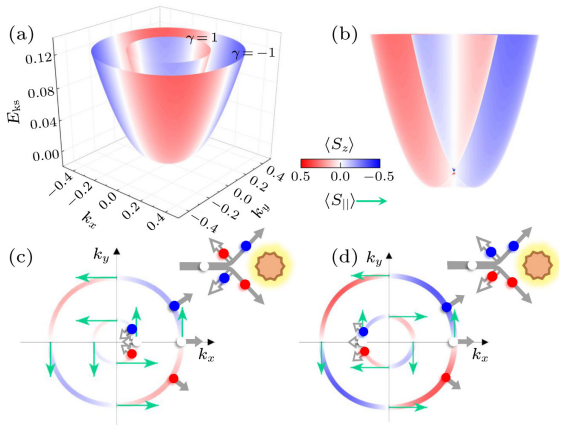

Fig. 1. (a) Dispersion relation of the Hamiltonian Eq. (1) with parameters $t_J = 0.2$ and $\lambda = 0.2$. (b) 2D projection of the dispersion relation at $k_y = 0$. The colormap indicates the value of the out-of-plane spin, $\langle s_z\rangle$. (c) and (d) Schematics of the Fermi surface cut below and above the Dirac point, respectively. Green arrows denote the in-plane spin texture of the Fermi-surface states, $\langle s_\parallel\rangle = (\langle s_x\rangle, \langle s_y\rangle)$, which satisfies $\langle s_x\rangle^2 + \langle s_y\rangle^2 + \langle s_z\rangle^2 = \hbar/2$. Gray arrows denote the particle velocity, with solid arrows corresponding to forward scattering states and hollow arrows to backward scattering states. Insets in (c) and (d) depict the schematics of forward and backward scattering processes in two cases. White, red, and blue solid circles represent quasiparticle states with $\langle s_z\rangle = 0, > 0$, and < 0.

Methods for Longitudinal and Spin Hall Conductivities. Within the framework of the quantum linear response theory, the longitudinal conductivity σ_{xx}^l and spin Hall conductivity σ_{yx}^s of electrons in a solid can be determined using the Kubo formalism:

$$\sigma_{ij}^{l/s} = \mathrm{Re}(\sigma_{ij}^{l/s,Ia} + \sigma_{ij}^{l/s,Ib} + \sigma_{ij}^{l/s,II}), \tag{5}$$

with

$$\begin{aligned} \sigma_{ij}^{l/s,Ia} &= \frac{e^2}{h}\int\frac{d^2\boldsymbol{k}}{(2\pi)^2}\mathrm{Tr}[v_i G_{\boldsymbol{k}}^R(E_\mathrm{F})v_j G_{\boldsymbol{k}}^A(E_\mathrm{F})]_c, \\ \sigma_{ij}^{l/s,Ib} &= -\frac{e^2}{h}\int\frac{d^2\boldsymbol{k}}{(2\pi)^2}\mathrm{Tr}[v_i G_{\boldsymbol{k}}^R(E_\mathrm{F})v_j G_{\boldsymbol{k}}^R(E_\mathrm{F})]_c, \\ \sigma_{ij}^{l/s,II} &= \frac{e^2}{h}\int dE f(E)\int\frac{d^2\boldsymbol{k}}{(2\pi)^2}\mathrm{Tr}\Big[v_i G_{\boldsymbol{k}}^R(E)v_j\frac{dG_{\boldsymbol{k}}^R(E)}{dE} \\ &\quad - v_i\frac{dG_{\boldsymbol{k}}^R(E)}{dE}v_j G_{\boldsymbol{k}}^R(E)\Big]_c. \end{aligned} \tag{6}$$

Here, $f(E) = \frac{1}{\exp[(E-E_\mathrm{F})/k_\mathrm{B}T]+1}$ is the Fermi–Dirac distribution function, Tr denotes the trace in the spin subspace, and the subscript c indicates the average disorder configuration. $G_{\boldsymbol{k}}^{R/A}(E) = 1/(E - H - \Sigma^{R/A})$ represents the retarded (R) and advanced (A) Green's functions of the disordered system with the self-energy function $\Sigma^{R/A}$. For the longitudinal conductivity (σ_{xx}^l), the vertices in the Kubo formula were set as $v_i = v_j = v_x$, whereas for the spin Hall conductivity (σ_{yx}^s), the vertices were set as $v_i = v_{s,y}$ and $v_j = v_x$. Clearly, $\sigma_{xx}^{l,II}$, which arises from the Fermi sea states, does not contribute to the longitudinal conductivity.

The Green functions in Eq. (6) can be expressed in the quasiparticle-state basis as $G_{\boldsymbol{k}}^{R/A}(E) = \mathrm{diag}[g_{+}^{R/A}(E), g_{-}^{R/A}(E)]$, where $g_{\pm}^{R/A}(E)$ is the retarded/advanced Green's function for the quasiparticle state with subband index $\gamma = \pm$. Given the δ-function disorder, the self-energy functions calculated using self-consistent Born's approximation (SCBA) are independent of both the momentum and the subband index γ. The real part of self-energy is neglected because it can be absorbed into the shifted energy levels. Subsequently, the quasiparticle-state Green's function is simplified to $g_{\gamma}^{R/A}(E) = 1/(E - E_{\boldsymbol{k}\gamma} \pm i/2\tau)$, where $\tau = -\hbar/2\mathrm{Im}\Sigma^{R}$ represents the quasiparticle relaxation time.

Three primary microscopic mechanisms—intrinsic, side-jump, and skew scattering—dominate the evaluation of the spin Hall effect.[35,36] The corresponding Feynman diagrams derived from the expansion of Kubo formalism are shown in Fig. 2.[36–41]

Intrinsic Mechanism. The intrinsic mechanism contributing to the longitudinal conductivity ($\sigma_{xx}^{l,\mathrm{int}}$) and spin Hall conductivity ($\sigma_{yx}^{s,\mathrm{int}}$) from the Fermi states is represented by the bubble Feynman diagram, as shown in Fig. 2(a). For $\sigma_{yx}^{s,\mathrm{int}}$, the intrinsic contribution from the Fermi sea states, that is $\sigma_{yx}^{s,II}$, should also be included. The numerical results of the spin Hall angle obtained from the intrinsic mechanism, denoted by $\sigma_{yx}^{s,\mathrm{int}}/\sigma_{xx}^{l,\mathrm{int}}$, are presented in Fig. 3 as a function of the charge density ratio n/n_0, where n and n_0 are the charge densities at the Fermi level and the Dirac point, respectively.

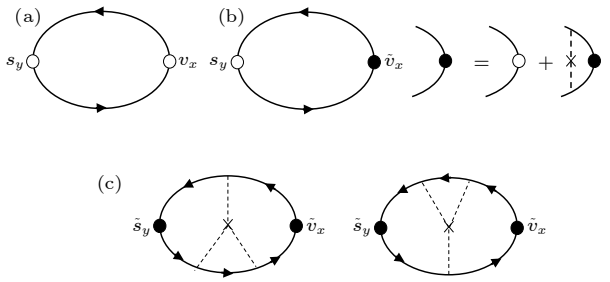

Fig. 2. Feynman diagrams illustrating mechanisms contributing to longitudinal and spin Hall conductivity: (a) Bubble diagram representing the intrinsic mechanism from the Fermi states. (b) Ladder-type vertex correction, indicative of the side-jump scattering mechanism. (c) Third-order single impurity vertex with current vertices modified by the ladder-type vertex correction, depicting skew scattering.[36,37]

Focusing on the region around the Dirac point ($k \ll \frac{\lambda}{t_J}$) and under conditions of weak disorder ($1/\tau \to 0$), the Kubo formula can be further simplified. Meanwhile, by decomposing the numerical results, we observed that the RR terms ($g^R g^R$), interband coherences ($g_+ g_-$ and $g_- g_+$), and the Fermi-sea contribution ($\sigma_{yx}^{s,II}$) can be almost neglected. Thus, $\sigma_{xx}^{l,\mathrm{int}}$ and $\sigma_{yx}^{s,\mathrm{int}}$ can be approximately obtained by

$$\sigma_{xx}^{l,\mathrm{int}} \approx \frac{\pi e^2 \tau}{h} \sum_{\gamma=\pm1} \int \frac{d^2\boldsymbol{k}}{(2\pi)^2} (v_x^{\gamma\gamma})^2 \delta(E - E_{\boldsymbol{k}\gamma}),$$
$$\sigma_{yx}^{s,\mathrm{int}} \approx \frac{\pi e^2 \tau}{h} \sum_{\gamma=\pm1} \int \frac{d^2\boldsymbol{k}}{(2\pi)^2} v_{s,y}^{\gamma\gamma} v_x^{\gamma\gamma} \delta(E - E_{\boldsymbol{k}\gamma}), \quad (7)$$

where

$$v_x^{\gamma\gamma} = \langle \boldsymbol{k}\gamma | v_x | \boldsymbol{k}\gamma \rangle \approx 2tk_x + \gamma \frac{\lambda k_x}{k},$$
$$v_{s,y}^{\gamma\gamma} = \langle \boldsymbol{k}\gamma | v_{s,y} | \boldsymbol{k}\gamma \rangle \approx 2t_J k_x + \gamma \frac{4tt_J k_y^2 k_x}{\lambda k}, \quad (8)$$

are the diagonal components of the charge and spin velocities in Eqs. (3) and (4). Plugging Eq. (8) into Eq. (7), we obtain

$$\sigma_{xx}^{l,\mathrm{int}} \approx \frac{e^2}{h} \frac{\lambda^2}{n_i V_0^2} \begin{cases} ll(\frac{n}{n_0})^2; & n < n_0, \\ 2(\frac{n}{n_0}) - 1; & n \geq n_0, \end{cases} \quad (9)$$

and

$$\sigma_{yx}^{s,\mathrm{int}} \approx \frac{e^2}{h} \frac{\lambda^2}{n_i V_0^2} \frac{t_J}{t} \begin{cases} \frac{5}{4}(\frac{n}{n_0})^2 - \frac{1}{4}(\frac{n}{n_0})^4; & n < n_0, \\ \frac{1}{2}(\frac{n}{n_0}) + \frac{1}{2}; & n \geq n_0. \end{cases} \quad (10)$$

Here, the relaxation time τ was obtained from the first-order Born's approximation. $\tau = \frac{2t}{V_0^2} \begin{cases} n/n_0; & n < n_0 \\ 1; & n \geq n_0 \end{cases}$. The charge density n was obtained in a pure system $n = \frac{\lambda^2}{2\pi t^2} \begin{cases} \sqrt{1 + 4tE_{\mathrm{F}}/\lambda^2}; & E_{\mathrm{F}} < 0 \\ 1 + 2tE_{\mathrm{F}}/\lambda^2; & E_{\mathrm{F}} \geq 0 \end{cases}$. Notably, in the absence of SOC ($\lambda = 0$), the Dirac point corresponds to the band edge, as shown in Fig. 1, which indicates that $n_0 = 0$. Thus, the small-momentum limit approximation $k \ll \frac{\lambda}{t_J}$ is inapplicable. In this case, the approximate analytical solutions for σ_{xx}^{l} and σ_{yx}^{s} are given by

$$\sigma_{xx}^{l}(\lambda{=}0) = t\frac{4\pi n e^2 \tau}{h}, \text{ and } \sigma_{yx}^{s}(\lambda{=}0) = t_J \frac{4\pi n e^2 \tau}{h}, \quad (11)$$

which differ from the results in Eqs. (9) and (10) with $\lambda = 0$, resulting in a spin Hall angle of $\sigma_{yx}^{s}/\sigma_{xx}^{l} = t_J/t$.

Side-jump scattering. The contribution of side-jump scattering corresponding to the ladder-type vertex correction in the Feynman diagrams is shown in Fig. 2(b), which can be obtained by solving the Bethe–Salpeter equation:

$$\tilde{v}_x^{LM}(\boldsymbol{k}, E) = v_x(\boldsymbol{k}) + V_0^2 \int \frac{d^2\boldsymbol{k}'}{(2\pi)^2} G_{\boldsymbol{k}'}^{L}(E) \tilde{v}_x^{LM}(\boldsymbol{k}', E) G_{\boldsymbol{k}'}^{M}(E), \quad (12)$$

where the subscripts L, $M = R$, A indicate the retarded or advanced quantities, respectively. The resolved dressed vertex is

$$\tilde{v}_x^{LM} = 2tk_x + 2t_J k_y \sigma_z + \lambda_c^{LM} \sigma_y \text{ with } \lambda_c^{LM} = \frac{1 + q_1^{LM}}{1 - q_2^{LM}} \lambda, \quad (13)$$

where

$$q_1^{LM} = \frac{V_0^2}{4} \int \frac{d^2\boldsymbol{k}}{(2\pi)^2} \Big[\frac{4tk_x^2}{d} (g_+^L g_+^M - g_-^L g_-^M) + \frac{8t_J^2 k_x^2 k_y^2}{d^2} (g_+^L - g_-^L)(g_+^M - g_-^M) + i\frac{4t_J k_y^2}{d} (g_+^L g_-^M - g_-^L g_+^M) \Big],$$
$$q_2^{LM} = \frac{V_0^2}{4} \int \frac{d^2\boldsymbol{k}}{(2\pi)^2} \Big[(g_+^L + g_-^L)(g_+^M + g_-^M) - \frac{4t_J^2 k_x^2 k_y^2}{d^2} (g_+^L - g_-^L)(g_+^M - g_-^M) \Big]. \quad (14)$$

A ladder-type correction was applied to the charge vertex by modifying v_x to $\tilde{v}_x$. Equivalently, a ladder-type correction can be applied to the spin vertex by modifying $v_{s,y}$ with $\tilde{v}_{s,y}$. Similarly, using the Bethe–Salpeter equation, we resolve the dressed spin vertex as

$$\tilde{v}_{s,y}^{LM} = 2t_J k_x + 2tk_y\sigma_z + \lambda_s^{LM}\sigma_y, \text{ with } \lambda_s^{LM} = \frac{q_{s1}^{LM}}{1-q_{s2}^{LM}}\lambda, \tag{15}$$

where

$$\begin{aligned} q_{s1}^{LM} = \frac{V_0^2}{4}\int \frac{d^2\boldsymbol{k}}{(2\pi)^2}\Big[&\frac{4t_J k_x^2}{d}(g_+^L g_+^M - g_-^L g_-^M) \\ &+ \frac{8tt_J k_x^2 k_y^2}{d^2}(g_+^L - g_-^L)(g_+^M - g_-^M) \\ &+ i\frac{4tk_y^2}{d}(g_+^L g_-^M - g_-^L g_+^M)\Big], \\ q_{s2}^{LM} = \frac{V_0^2}{4}\int \frac{d^2\boldsymbol{k}}{(2\pi)^2}\Big[&(g_+^L + g_-^L)(g_+^M + g_-^M) \\ &- \frac{4t_J^2 k_x^2 k_y^2}{d^2}(g_+^L - g_-^L)(g_+^M - g_-^M)\Big]. \end{aligned} \tag{16}$$

Therefore, the longitudinal ($\sigma_{xx}^{l,\mathrm{int+sj}}$) and spin Hall ($\sigma_{yx}^{s,\mathrm{int+sj}}$) conductivities, which include both intrinsic and side-jump scattering contributions, can be evaluated by replacing one vertex with that dressed by the ladder-type correction in the Kubo formula Eq. (6). For $\sigma_{xx}^{l,\mathrm{int+sj}}$, one charge vertex v_x can be replaced with $\tilde{v}_x$; for $\sigma_{yx}^{s,\mathrm{int+sj}}$, the charge vertex v_x can be replaced with $\tilde{v}_x$ or the spin vertex $v_{s,y}$ with $\tilde{v}_{s,y}$.

Similarly, we can derive the analytical solutions for $\sigma_{xx}^{l,\mathrm{int+sj}}$ and $\sigma_{yx}^{s,\mathrm{int+sj}}$ in the limits $k \ll \frac{\lambda}{t_J}$ and $1/\tau \to 0$ while neglecting the RR terms ($g^R g^R$), the interband coherences ($g_+ g_-$, $g_- g_+$), and the Fermi-sea contribution ($\sigma_{yx}^{s,II}$). These solutions were approximately obtained using

$$\begin{aligned} \sigma_{xx}^{l,\mathrm{int+sj}} &\approx \frac{\pi e^2\tau}{h}\sum_{\gamma=\pm}\int \frac{d^2\boldsymbol{k}}{(2\pi)^2} v_x^{\gamma\gamma}\tilde{v}_x^{\gamma\gamma}\delta(E - E_{\boldsymbol{k}\gamma}), \\ \sigma_{yx}^{s,\mathrm{int+sj}} &\approx \frac{\pi e^2\tau}{h}\sum_{\gamma=\pm}\int \frac{d^2\boldsymbol{k}}{(2\pi)^2} v_{s,y}^{\gamma\gamma}\tilde{v}_x^{\gamma\gamma}\delta(E - E_{\boldsymbol{k}\gamma}), \end{aligned} \tag{17}$$

where

$$\tilde{v}_x^{\gamma\gamma} = 2tk_x + \gamma\frac{\lambda^{RA}k_x}{k} \text{ with } \lambda^{RA} = \begin{cases} -\frac{4tE}{\lambda}; & E < 0, \\ 0; & E \geq 0, \end{cases} \tag{18}$$

is the diagonal component of the dressed charge velocity obtained from Eq. (13), which corresponds to the renormalized quasiparticle velocity. Plugging Eqs. (8) and (18) into Eq. (17), we obtain the analytical solutions

$$\sigma_{xx}^{l,\mathrm{int+sj}} = \frac{e^2}{h}\frac{2\lambda^2}{n_i V_0^2}\begin{cases} \frac{1}{2}[(\frac{n}{n_0})^4 + (\frac{n}{n_0})^2]; & n < n_0, \\ (\frac{n}{n_0}); & n \geq n_0, \end{cases} \tag{19}$$

and

$$\sigma_{yx}^{s,\mathrm{int+sj}} = \frac{e^2}{h}\frac{2\lambda^2}{n_i V_0^2}\frac{t_J}{t}\begin{cases} \frac{n}{n_0}; & n < n_0, \\ 1; & n \geq n_0. \end{cases} \tag{20}$$

In contrast to the intrinsic contribution, an analysis of the parities of k_x and k_y in Eq. (17) reveals that the side-jump scattering contribution vanishes in the absence of SOC ($\lambda = 0$).

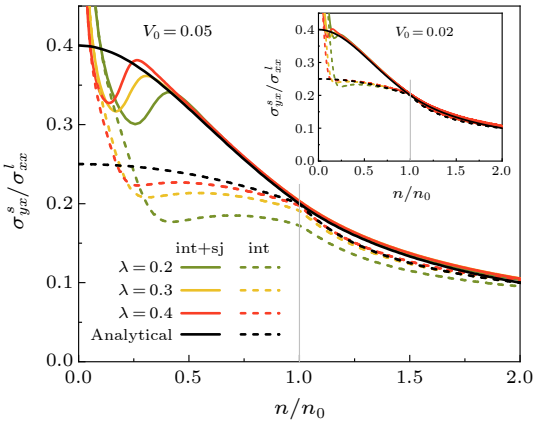

Fig. 3. Numerical and analytical results of the spin Hall angle of the 2D Rashba altermagnet around the Dirac point with different SOC strengths λ. Dashed lines indicate contributions solely from the intrinsic mechanism, while solid lines incorporate both the intrinsic and side-jump mechanisms. Analytical solutions, depicted by black dashed and solid lines, are obtained from Eqs. [(9)-(10)] and [(19)-(20)]. Other parameters: $t_J = 0.2$ and $V_0 = 0.05$ (main panel), 0.02 (inset). The charge density ratio corresponding to the Dirac point ($n/n_0 = 1$) is indicated by a gray line.

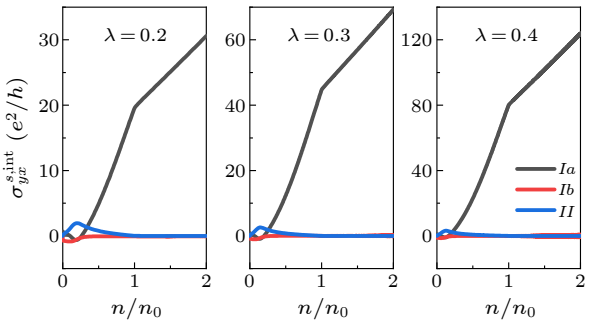

Fig. 4. Numerical results for the spin Hall conductivity components $\sigma_{yx}^{s,Ia}$, $\sigma_{yx}^{s,Ib}$, and $\sigma_{yx}^{s,II}$ contributed by the intrinsic mechanism at SOC strengths of $\lambda = 0.2$, $\lambda = 0.3$, and $\lambda = 0.4$. Other parameters: $t_J = 0.2$ and $V_0 = 0.02$.

In Fig. 3, we present the numerical and analytical results for the spin Hall angle, including the contributions from both the intrinsic and side-jump scattering mechanisms, $\sigma_{yx}^{s,\mathrm{int+sj}}/\sigma_{xx}^{l,\mathrm{int+sj}}$, as a function of n/n_0, compared with the results considering only the intrinsic mechanism. We found that below the Dirac point ($n/n_0 < 1$), the spin Hall angle can be significantly enhanced by side-jump scattering, whereas above the Dirac point ($n/n_0 > 1$), the spin Hall angle shows almost no change with or without the side-jump scattering contribution. Additionally, when the Fermi energy is very close to the band edge or when subband overlap occurs because of disorder, the RR terms ($g^R g^R$) and interband coherence ($g_+ g_-$, $g_- g_+$) terms become important, resulting in the spin Hall angle being dependent on λ, which is absent in the analytical solution. As the disorder strength decreases, the numerical results converge toward the analytical solution, as shown in the inset of Fig. 3 for $V_0 = 0.02$. Similarly, we found that the

contribution from the Fermi sea states ($\sigma_{yx}^{s,II}$) is significantly smaller than that from the Fermi states ($\sigma_{yx}^{s,Ia}$) and is confined to regions extremely close to the band edge, as shown in Fig. 4. This negligible contribution of $\sigma_{yx}^{s,\mathrm{int}}$ may be attributed to the Berry curvature integral over the Fermi sea being zero, because contributions from Fermi sea states are often associated with the topological characteristics of the band structure.

The analytically derived renormalized quasiparticle velocity given by Eq. (18) is the same as that obtained for the 2D Rashba electron gas without altering the magnetic exchange interaction.[31,42] This correspondence indicates that the side-jump mechanism effectively suppresses backward-scattering processes in a manner similar to that discussed in Ref. [31], where spin conservation inhibits backscattering between states with the same Fermi energy but located on different Fermi circles. In the system considered in this study, such suppression stems from the helicity-driven orthogonality between the in-plane spins of states with antiparallel velocities and momenta. Consequently, regardless of the Fermi energy location relative to the Dirac point, backward scattering predominantly occurs between quasiparticle states across different Fermi circles, reversing the quasiparticle velocity's sign without altering the momentum direction, as illustrated schematically in the insets of Figs. 1(c) and 1(d).

Unlike the longitudinal conductivity, the spin Hall conductivity, which is primarily influenced by the distribution of transport states, is also affected by the polarization of the out-of-plane spin $\langle s_z\rangle$. Above the Dirac point, the polarization direction of $\langle s_z\rangle$ in the backward-scattering state is parallel to that in the forward-scattering state but antiparallel below the Dirac point. Consequently, suppressing backward scattering below the Dirac point not only increases the distribution of transport states but also enhances the $\langle s_z\rangle$ polarization. This dual-enhancement effect significantly boosts the spin Hall conductivity, significantly increasing the spin Hall angle.

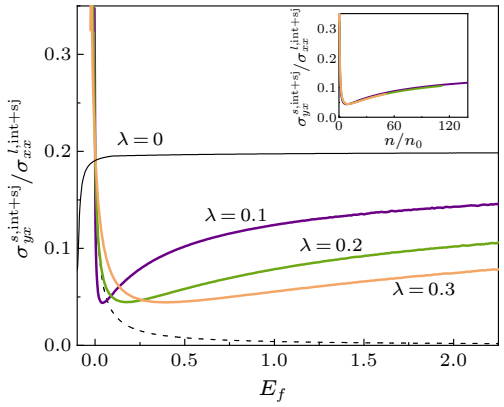

Fig. 5. $\sigma_{yx}^{s,\mathrm{int+sj}}/\sigma_{xx}^{l,\mathrm{int+sj}}$ as a function of E_f across a broad energy scale. Parameters: $t_J=0.2$, $\lambda=0$ (black), 0.1 (purple), 0.2 (green), 0.3 (orange), and $V_0=0.05$. The dashed line denotes the analytical result given by Eqs. (19 and 20). The inset shows the numerical results for $\lambda=0.1$ (purple), 0.2 (green), and 0.3 (orange) as a function of n/n_0.

In Fig. 5, we present $\sigma_{yx}^{s,\mathrm{int+sj}}/\sigma_{xx}^{l,\mathrm{int+sj}}$ as a function of E_f over a broad range of values. The numerical results deviate from the analytical solutions provided by Eqs. [(19)-(20)] in the high-energy region because of the assumption that $k\ll\frac{\lambda}{t_J}$ is no longer valid. However, for $\lambda=0$, the numerical results agree well with the analytical solution presented in Eq. (11), which was specifically derived for the limit $\lambda=0$. Comparing the results for $\lambda=0$ with those for $\lambda\neq 0$, we found that the SOC effect suppresses the spin Hall angle in the region above the Dirac point; however, this suppression weakens with increasing E_f. This trend is linked to the decrease in the in-plane spin component $\langle s_\parallel\rangle$, as shown in Fig. 1, which consequently diminishes the influence of SOC-induced helical spin textures on the spin Hall effect. Furthermore, we found that the dependence of the spin Hall angle on parameter λ almost disappears in the high-energy regime after scaling by replacing E_f with n/n_0, as shown in the inset of Fig. 5.

Skew Scattering. The contribution from skew scattering was evaluated using Feynman diagrams with a single third-order impurity vertex and both external velocity vertices renormalized by ladder-type vertex corrections, as shown in Fig. 2(c). From these diagrams, the longitudinal ($\sigma_{xx}^{l,\mathrm{skew}}$) and spin Hall ($\sigma_{yx}^{s,\mathrm{skew}}$) conductivities resulting from skew scattering are given by

$$\sigma_{ij}^{l/s,\mathrm{skew}}=\mathrm{Re}(\sigma_{ij}^{l/s,Ia,\mathrm{skew}}+\sigma_{ij}^{l/s,Ib,\mathrm{skew}}), \tag{21}$$

with

$$\begin{aligned}\sigma_{ij}^{l/s,Ia,\mathrm{skew}}&=\frac{e^2}{h}V_1^3\int\frac{d^2\boldsymbol{k}}{(2\pi)^2}\mathrm{Tr}[\tilde{v}_i^{AR}G_{\boldsymbol{k}}^R\tilde{v}_j^{RA}+\tilde{v}_i^{AR}\tilde{v}_j^{RA}G_{\boldsymbol{k}}^A],\\ \sigma_{ij}^{l/s,Ib,\mathrm{skew}}&=-\frac{e^2}{h}V_1^3\mathrm{Re}\int\frac{d^2\boldsymbol{k}}{(2\pi)^2}\mathrm{Tr}[\tilde{v}_i^{RR}G_{\boldsymbol{k}}^R\tilde{v}_j^{RR}\\ &\quad+\tilde{v}_i^{RR}\tilde{v}_j^{RR}G_{\boldsymbol{k}}^R],\end{aligned} \tag{22}$$

where the vertices are set as $\tilde{v}_i^{LM}=\tilde{v}_j^{LM}=\tilde{v}_x^{LM}$ for $\sigma_{xx}^{l,\mathrm{skew}}$, and set as $\tilde{v}_i^{LM}=\tilde{v}_{s,y}^{LM}$ and $\tilde{v}_j^{LM}=\tilde{v}_x^{LM}$ for $\sigma_{yx}^{s,\mathrm{skew}}$.

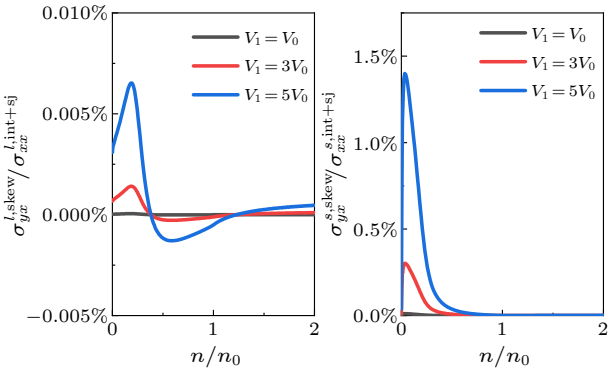

Fig. 6. Ratio of the skew scattering contribution to the intrinsic and side-jump scattering contributions for both the longitudinal and spin Hall conductivities. Other parameters: $t_J=0.2$, $\lambda=0.3$, and $V_0=0.05$.

Numerical calculations revealed that the contribution of skew scattering to these conductivities is negligible compared to those from the intrinsic and side-jump scattering mechanisms, even for a large V_1, as shown in

Fig. 6. This finding contrasts with conventional ferromagnetic systems with Rashba SOCs, where skew scattering significantly affects both the anomalous and spin Hall conductivities when third-order disorder correlators are considered.[37,43,44] The key difference lies in the altermagnetic exchange interaction that breaks the time-reversal symmetry without inducing asymmetry in the lifetimes of quasiparticle states across the two subbands.

Discussion and Conclusion. We explored the charge-to-spin conversion in 2D Rashba altermagnets by calculating the spin Hall angle using the quantum linear response theory. We found that the side-jump mechanism could markedly enhance the spin Hall conductivity below the band-crossing point, thereby facilitating the achievement of a large spin Hall angle. By analyzing the in-plane and out-of-plane spin textures, we demonstrated that the side-jump mechanism produces a dual-enhancement effect on the generation of spin current in this region, suppressing backward scattering and increasing spin polarization. Furthermore, we found that away from the Dirac point, the impact of SOC-induced helical spin textures on the spin Hall effect was reduced owing to a reduction in the in-plane spin component.

The concluding remarks are as follows: First, our findings propose a novel strategy for manipulating charge-to-spin conversion through sophisticated control of in-plane and out-of-plane spin textures, providing insights into further high-efficiency conversion in altermagnets. Second, there has been a significant increase in reports on 2D magnetic materials characterized by marked anisotropic spin splitting and strong SOC,[45–49] which are suitable platforms for achieving our idea. Third, in contrast to typical ferromagnetic Rashba systems, the skew scattering mechanism and intrinsic mechanism arising from Fermi sea states are almost negligible in this system, which can be attributed to the unique time-reversal symmetry breaking in altermagnets. Therefore, our research is expected to pave the way for further investigations into the uniqueness of time-reversal symmetry breaking in altermagnetic materials, potentially expanding the scope of their applications in spintronics. Fourth, the Rashba SOC in our effective model, which typically originates from the asymmetry of the potential along the out-of-plane direction, explicitly breaks the parity symmetry (P). In contrast, SOCs that preserve both time reversal (T) and parity symmetry (P), such as those found in PT-symmetric antiferromagnets, require at least a 4×4 effective Hamiltonian to adequately capture the relevant physics.

Acknowledgement. This work was supported by the National Key R&D Program (Grant No. 2022YFA1402204) and the National Natural Science Foundation of China (Grant No. 52471020).

References

[1] Wu C and Zhang S C 2004 *Phys. Rev. Lett.* **93** 036403
[2] Wu C, Sun K, Fradkin E, and Zhang S C 2007 *Phys. Rev. B* **75** 115103
[3] Smejkal L, Sinova J, and Jungwirth T 2022 *Phys. Rev. X* **12** 040501
[4] Smejkal L, MacDonald A H, Sinova J, Nakatsuji S, and Jungwirth T 2022 *Nat. Rev. Mater.* **7** 482
[5] Ouassou J A, Brataas A, and Linder J 2023 *Phys. Rev. Lett.* **131** 076003
[6] Smejkal L, Sinova J, and Jungwirth T 2022 *Phys. Rev. X* **12** 031042
[7] Bai H, Zhang Y C, Zhou Y J, Chen P, Wan C H, Han L, Zhu W X, Liang S X, Su Y C, Han X F, Pan F, and Song C 2023 *Phys. Rev. Lett.* **130** 216701
[8] Krempaský J, Šmejkal L, D'Souza S W, Hajlaoui M, Springholz G, Uhlířová K, Alarab F, Constantinou P C, Strocov V, Usanov D, Pudelko W R, Hernández R G, Hellenes A B, Jansa Z, Reichlová H, Šobáň Z, Betancourt R D G, P. Wadley, Sinova J, Kriegner D, Minár J, Dil J H, and Jungwirth T 2024 *Nature* **626** 517
[9] Šmejkal L, Hernández R G, Jungwirth T, and Sinova J 2020 *Sci. Adv.* **6** eaaz8809
[10] Osumi T, Souma S, Aoyama T, Yamauchi K, Honma A, Nakayama K, Takahashi T, Ohgushi K, and Sato T 2024 *Phys. Rev. B* **109** 115102
[11] Hernández R G, Šmejkal L, Výborný K, Yahagi Y, Sinova J, Jungwirth T, and Železný J 2021 *Phys. Rev. Lett.* **126** 127701
[12] Bai H, Han L, Feng X Y, Zhou Y J, Su R X, Wang Q, Liao L Y, ZhuW X, Chen X Z, Pan F, Fan X L, and Song C 2022 *Phys. Rev. Lett.* **128** 197202
[13] Naka M, Motome Y, and Seo H 2021 *Phys. Rev. B* **103** 125114
[14] Naka M, Hayami S, Kusunose H, Yanagi Y, Motome Y, and Seo H 2019 *Nat. Commun.* **10** 4305
[15] Li Z, Zhang Z, Lu X, and Xu Y 2024 arXiv:2407.07447 [physics.app-ph]
[16] Ma H Y, Hu M, Li N, Liu J, Yao W, Jia J F, and Liu J 2021 *Nat. Commun.* **12** 2846
[17] Karube S, Tanaka T, Sugawara D, Kadoguchi N, Kohda M, and Nitta J 2022 *Phys. Rev. Lett.* **129** 137201
[18] Reimers S, Odenbreit L, Šmejkal L, Strocov V N, Constantinou P, Hellenes A B, Ubiergo R J, Campos W H, Bharadwaj V K, Chakraborty A, Denneulin T, Shi W, Borkowski R E D, Das S, Kläui M, Sinova J, and Jourdan M 2024 *Nat. Commun.* **15** 2116
[19] Hayami S, Yanagi Y, and Kusunose H 2019 *J. Phys. Soc. Jpn.* **88** 123702
[20] Hayami S, Yanagi Y, and Kusunose H 2020 *Phys. Rev. B* **102** 144441
[21] Reichlova H, Seeger R L, Hernández R G, Kounta I, Schlitz R, Kriegner D, Ritzinger P, Lammel M, Leiviskä M, Hellenes A B, Olejnik K, Petŭiček V, Doležal P, Horak L, Schmoranzerova E, Badura A, Bertaina S, Thomas A, Baltz V, Michez L, Sinova J, Goennenwein S T B, Jungwirth T, and Šmejkal L 2024 *Nat. Commun.* **15** 4961
[22] Sasabe N, Mizumaki M, Uozumi T, and Yamasaki Y 2023 *Phys. Rev. Lett.* **131** 216501
[23] Seo S, Hayami S, Su Y, Thomas S M, Ronning F, Bauer E D, Thompson J D, Lin S Z, and Rosa P F S 2021 *Commun. Phys.* **4** 58
[24] Hua J, Wang Z F, Zhu W, and Chen W 2024 *Phys. Rev. B* **109** 115429
[25] Gorini C, Schwab P, Dzierzawa M, and Raimondi R 2008 *Phys. Rev. B* **78** 125327
[26] Chen Y, Du Z Z, Lu H Z, and Xie X C 2024 *Phys. Rev. B* **109** L121115
[27] Zhu M, Dong J, Li X, Zheng F, Zhou Y, Wu K, and Zhang J 2024 *Chin. Phys. Lett.* **41** 047502
[28] Zhu Y, Zhao B, Xue Y, Xu W, Xu W, and Yang Z 2024 *Chin. Phys. Lett.* **41** 067301
[29] Šmejkal L, Hellenes A B, Hernández R G, Sinova J, and Jungwirth T 2022 *Phys. Rev. X* **12** 011028

[30] Cui Q, Zhu Y, Yao X, Cui P, and Yang H 2023 *Phys. Rev. B* **108** 024410
[31] Brosco V, Benfatto L, Cappelluti E, and Grimaldi C 2016 *Phys. Rev. Lett.* **116** 166602
[32] Rashba E I 2004 *Phys. Rev. B* **70** 201309
[33] Dimitrova O V 2005 *Phys. Rev. B* **71** 245327
[34] Grimaldi C, Cappelluti E, and Marsiglio F 2006 *Phys. Rev. B* **73** 081303
[35] Sinova J, Valenzuela S O, Wunderlich J, Back C H, and Jungwirth T 2015 *Rev. Mod. Phys.* **87** 1213
[36] Tse W K and Sarma S Das 2006 *Phys. Rev. B* **74** 245309
[37] Nunner T S, Zaránd G, and Oppen F 2008 *Phys. Rev. Lett.* **100** 236602
[38] Borunda M, Nunner T S, Luck T, Sinitsyn N A, Timm C, Wunderlich J, Jungwirth T, MacDonald A H, and Sinova J 2007 *Phys. Rev. Lett.* **99** 066604
[39] Nunner T S, Sinitsyn N A, Borunda M F, Dugaev V K, Kovalev A A, Abanov A, Timm C, Jungwirth T, Inoue J, MacDonald A H, and Sinova J 2007 *Phys. Rev. B* **76** 235312
[40] Kovalev A A, Tserkovnyak Y, Výborný K, and Sinova J 2009 *Phys. Rev. B* **79** 195129
[41] Yang S A, Pan H, Yao Y, and Niu Q 2011 *Phys. Rev. B* **83** 125122
[42] Chen W, Xiao C, Shi Q, and Li Q 2020 *Phys. Rev. B* **101** 020203
[43] Sinova J, Culcer D, Niu Q, Sinitsyn N A, Jungwirth T, and Mac-Donald A H 2004 *Phys. Rev. Lett.* **92** 126603
[44] Onoda S, Sugimoto N, and Nagaosa N 2006 *Phys. Rev. Lett.* **97** 126602
[45] Liu Q, Kang J, Wang P, Gao W, Qi Y, Zhao J and Jiang X 2024 *Adv. Funct. Mater.* **34** 2402080
[46] Sødequist J and Olsen T 2024 *Appl. Phys. Lett.* **124** 182409
[47] Parfenov O E, Averyanov D V, Sokolov I S, Mihalyuk A N, Kondratev O A, Taldenkov A N, Tokmachev A M, and Storchak V G 2024 arXiv:2406.07172 [cond-mat.mtrl-sci]
[48] Mazin I, Hernández R G, and Šmejkal L 2023 arXiv:2309.02355 [cond-mat.mes-hall]
[49] Wu Y, Deng L, Yin X, Tong J, Tian F, and Zhang X 2024 *Nano. Lett.* **24** 10534